Environmental Research Letters

CrossMark

LETTER

Stronger warming amplification over drier ecoregions observed since 1979

Liming Zhou[1], Haishan Chen[2] and Yongjiu Dai[3]

[1]   Department of Atmospheric and Environmental Sciences, SUNY at Albany, Albany, NY 12222, USA
[2]   Key Laboratory of Meteorological Disaster of Ministry of Education, Nanjing University of Information Science and Technology, Nanjing 210044, People's Republic of China
[3]   College of Global Change and Earth System Science, Beijing Normal University, Beijing, 100875, People's Republic of China

E-mail: lzhou@albany.edu

Abstract

Observations show that the global mean surface temperature has increased steadily since the 1950s and this warming trend is particularly strong and linear over land after 1979. This paper analyzes the relationship between surface temperature trends observed over land for the period 1979–2012 and enhanced vegetation index (EVI), a satellite measured vegetation greenness index, by large-scale ecoregion. The land areas between 50°S and 50°N are classified into various large-scale ecoregions based on the climatological EVI values. The regional mean temperature trends exhibit significant spatial dependence on the regional mean EVI. In general, the warming rate increases dramatically with decreasing EVI, with the strongest warming rate seen over the driest ecoregions. When anthropogenic and natural forcings are included, climate models are generally able to reproduce observed major features of the spatial dependence. When only natural forcings are used, none of the observed features are simulated. Furthermore, the simulated temperature changes in the latter are mostly far outside the range of those in the former. These results suggest stronger warming amplification over drier ecoregions in the context of global warming, pointing mainly to human influence.

1. Introduction

The global mean surface temperature has increased by about 0.85 °C since 1880 and much of the warming has occurred in the last several decades (IPCC 2013). Both observations and model simulations have attributed the global warming since 1950 mostly to the increase in anthropogenic greenhouse gases (GHGs) in the atmosphere (IPCC 2013). The GHGs-induced positive radiative forcing is global-scale and roughly spatially uniform but can be amplified or dampened by various feedbacks at regional scales (Hansen *et al* 2010, Thorne *et al* 2011). For example, the warming is much greater over land than oceans, over higher latitudes (Lu and Cai 2010) and over higher elevations (e.g., Naud *et al* 2013, Rangwala *et al* 2013).

Over non-polar land surfaces, the warming rate differs substantially among ecosystems due to their differences in thermal and hydrological properties.

The GHGs-induced positive radiative forcing at the surface can be largely weakened by evapotranspiration (ET) with increasing amounts of vegetation and soil moisture (Koster *et al* 2004, 2009, Zhou *et al* 2007, Jeong *et al* 2009, Georgescu *et al* 2011). Lim *et al* (2005) showed that the warming rate is larger for barren lands. Zhou *et al* (2007, 2009, 2010) found that the warming trend of minimum temperature and the decreasing trend of diurnal temperature range are stronger over drier regions. ET is a primary process driving energy and water exchanges between the hydrosphere, atmosphere and biosphere (Wang and Dickinson 2012) in regions where soil moisture is the main controlling factor for ET. With decreasing soil moisture content, particularly over very dry ecosystems, the soil moisture–ET coupling weakens dramatically. Thus, such spatial variations of ET may determine surface warming rates among different ecosystems. However, few studies have

quantified such spatial variations in the warming rates over land.

Quantifying and attributing this spatial dependence is important for understanding climate sensitivity to anthropogenic forcings, uncovering mechanisms of spatiotemporal patterns of climate change, and assessing climatic impacts. Here we use the enhanced vegetation index (EVI), an optimized vegetation greenness index measured by the MODerate resolution Imaging Spectroradiometer (MODIS) satellite sensor (Huete *et al* 2002), to examine the spatial dependence of observed surface warming rates on large-scale ecoregions. Similar analyses are also performed to historical simulations of global coupled atmosphere-ocean general circulation models (AOGCMs) developed for the Coupled Model Intercomparison Project phase 5 (CMIP5) (Taylor *et al* 2012), which are generally able to reproduce the observed warming, especially after the 1950s (Simmons *et al* 2010, IPCC 2013). EVI does not saturate, even over dense forests, and correlates highly with ET, particularly at large scales (Suzuki and Masuda 2004, Nagler *et al* 2005). This study focuses only on the modern satellite data era for the period 1979–2012 to maximize spatial coverage of measurements. Furthermore, after adjusting observations to remove the estimated impacts of known factors on short-term temperature variations, the global warming signal from 1979 through 2010 is particularly strong and steadily linear (Foster and Rahmstorf 2011).

2. Data and methods

This study uses the most recent versions of global gridded monthly surface air temperature (T) datasets: CRU (Harris and Jones 2014), GISS (Hansen *et al* 2010) and NCDC (Vose *et al* 2012) for the period 1979–2012, which have been widely used for long-term T variability and trend analysis. Despite sharing some similarities in input data sources, these three datasets differ substantially in their data processing approaches. For example, satellite data is used extensively in GISS, used very limited in NCDC, and not used at all in CRU (Vose *et al* 2012). In addition, monthly data of GPCP precipitation (Adler *et al* 2003) for the period 1979–2012 and MODIS EVI (Huete *et al* 2002) for the period 2000–2012 are also used. More specifics of each dataset are detailed in supplementary table S1.
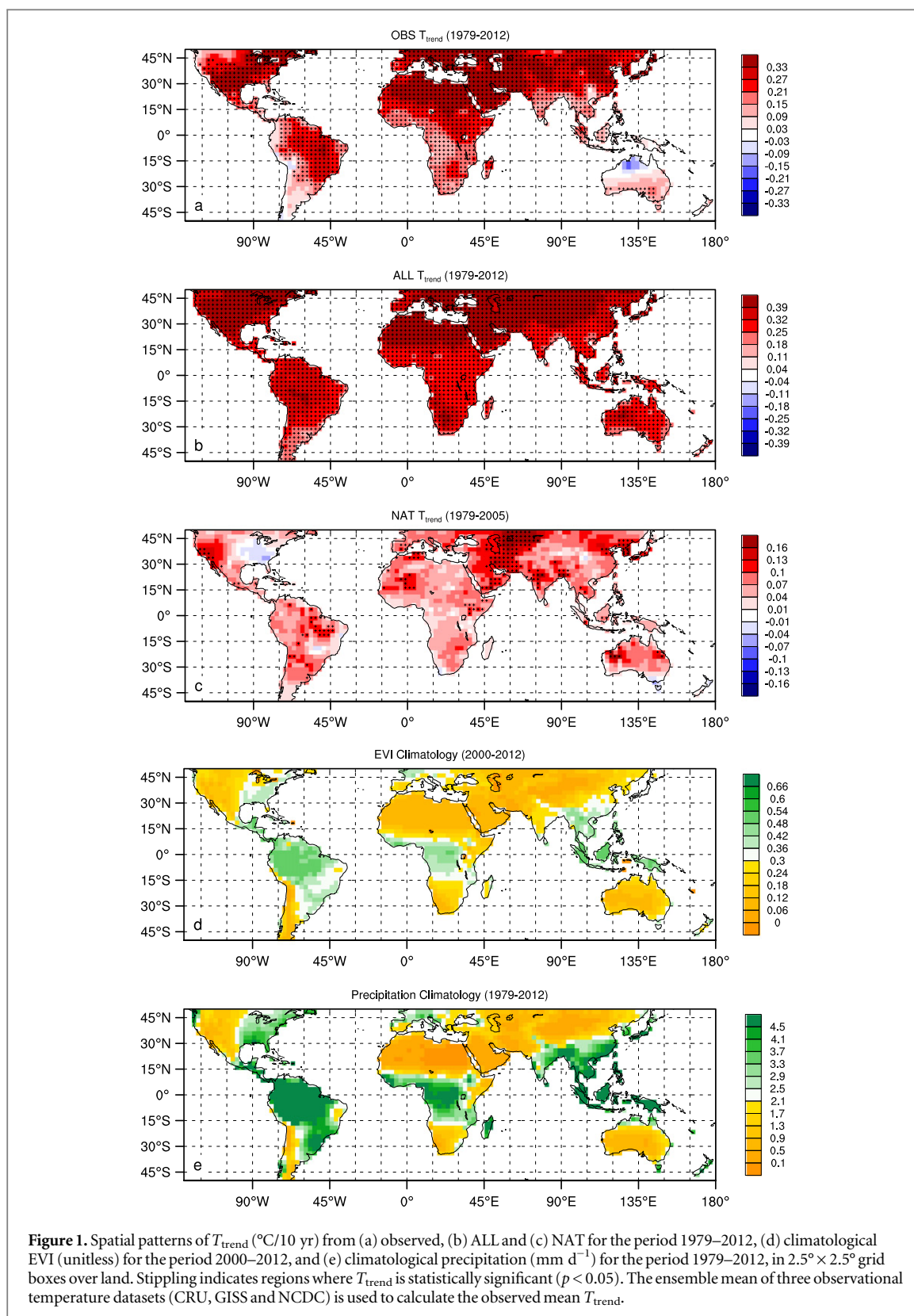
We analyze monthly output of historical simulations from the CMIP5 archives, which include time-evolving changes in anthropogenic (GHGs and sulfate aerosols) and/or natural (solar and volcanic) forcing agents for the period 1860–2006, extended for the years 2006–2012 with the RCP4.5 scenario runs. These simulations are divided into two groups: one with anthropogenic and natural forcings (referred to as ALL) and the other with only natural forcings (referred to as NAT). Although most of CMIP5 models have performed multi-member ensemble runs, we choose

only one ensemble 'r1i1p1' from 12 AOGCMs (supplementary table S2) that have required variables in ALL, NAT and RCP45 simulations. As averaging over multiple members enhances the forcing signal and reduces noise from internal variability and errors from individual models, we simply average the 12 simulations to obtain the multi-model ensemble mean for the period 1979–2012 in ALL and the period 1979–2005 in NAT.

All variables are spatially re-projected into grid boxes of 2.5° latitude by 2.5° longitude. The monthly EVI and precipitation are aggregated to create the annual climatology, and the monthly temperatures are temporally averaged to generate annual mean anomalies. For a time series at a given grid box, a linear trend is estimated using least squares fitting and a two-tailed student's t test is used to test whether the trend differs significantly from zero. For simplicity, we refer to the temperature trend as T_{trend}.

We focus only on the land areas that have at least 10 months of data for each year and at least 26 years of data (i.e., 75%) during the period 1979–2012 in all three observational T datasets following the selection criteria of Vose *et al* (2012). The land beyond 50°N and 50°S is excluded to minimize snow/ice-albedo feedbacks that dominate the high-latitude warming. Annual mean T anomalies are used to maximize large-scale long-term T trends as the GHGs-induced radiative forcing is likely a dominant driver on these scales (e.g., Zhou *et al* 2007, 2009, 2010). Seasonal or monthly T anomalies are also affected by other factors such as sea surface temperature (Cohen *et al* 2012) and cloud cover (Tang and Leng 2013). The three datasets show similar T changes and thus their ensemble mean is mostly used to reduce redundancy. In addition, only those grids with annual T_{trend} that is statistically significant ($p < 0.1$) are considered to exclude regions with no trends or unrealistic trends due to data uncertainties or gaps. In total, among the 1537 land grid boxes of 2.5° by 2.5° between 50°S and 50°N, 1338 are considered as the study region. CMIP5 simulations are sampled so that coverage corresponds to that of the observations.

This study evaluates T_{trend} at the aggregated large-scale level to minimize grid-level data noise and variability. We classify the 1338 grids into 7, 14, 21, 28, and 35 large-scale ecoregions from barren to dense vegetation based on the climatological EVI values (referred to as $\overline{\text{EVI}}$), and then analyze how T_{trend} varies with $\overline{\text{EVI}}$ by ecoregion via least squares fitting. The goodness of fit (R^2) is used to measure how successful the fit is in approximating the fraction of the data variations. Different classifications are used to test whether the fitted $T_{\text{trend}} - \overline{\text{EVI}}$ relationship is robust. For each classification, every ecoregion contains about the same number of grid boxes. The regional mean time series is calculated using area-weighted averaging over land grids within each ecoregion, and its trend is estimated as done at the grid level. For brevity, only results of 7 and 35 ecoregions, which represent the least and most
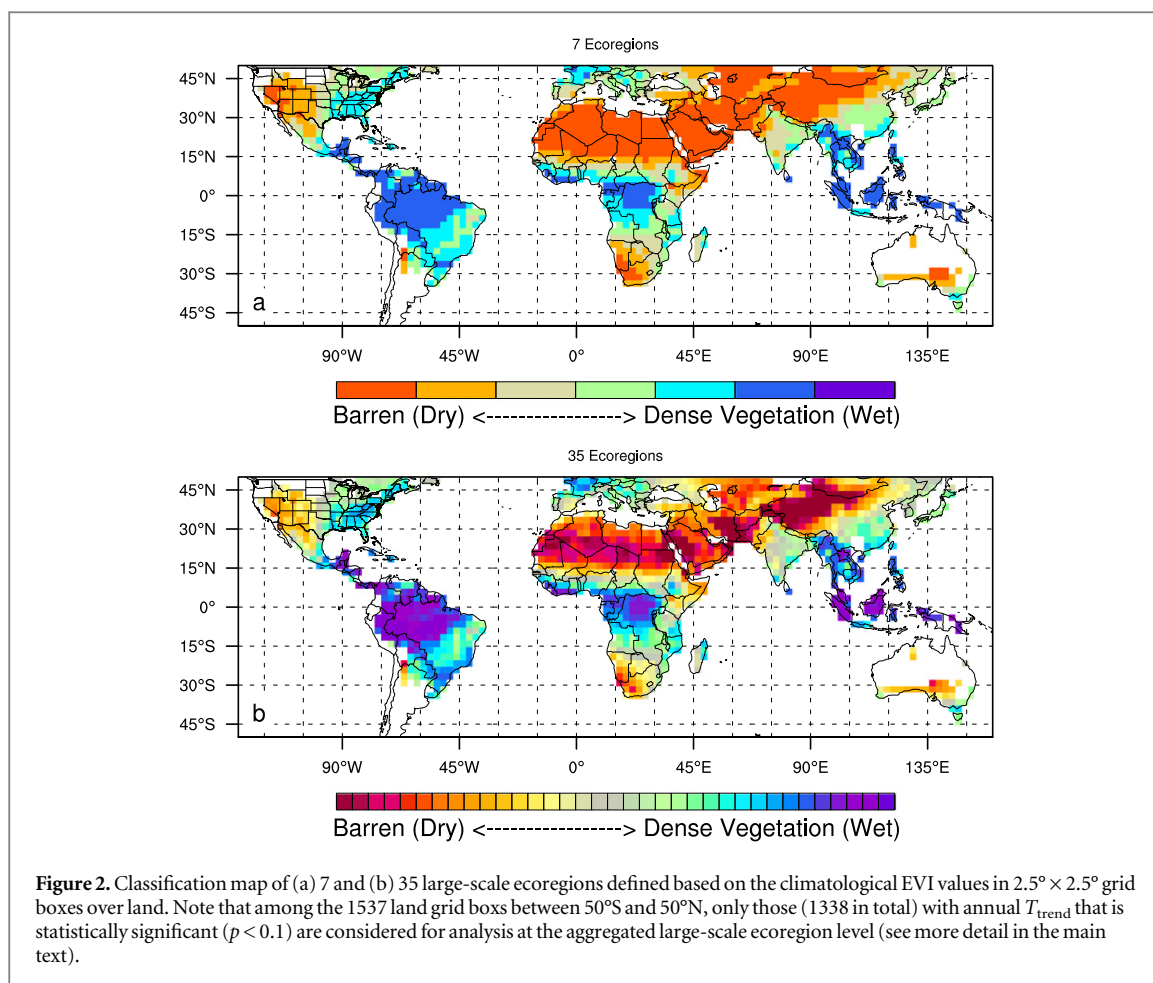
Figure 1. Spatial patterns of T_{trend} (°C/10 yr) from (a) observed, (b) ALL and (c) NAT for the period 1979–2012, (d) climatological EVI (unitless) for the period 2000–2012, and (e) climatological precipitation (mm d^{-1}) for the period 1979–2012, in 2.5° × 2.5° grid boxes over land. Stippling indicates regions where T_{trend} is statistically significant ($p < 0.05$). The ensemble mean of three observational temperature datasets (CRU, GISS and NCDC) is used to calculate the observed mean T_{trend}.

ecoregions classified, are shown in figures, while those of other classifications are listed in tables.

3. Results

3.1. Observational temperature trends

Figure 1(a) shows the observed T_{trend} over all the 1537 land grids between 50°S and 50°N for the period

1979–2012, together with the climatology of EVI (figure 1(d)) and precipitation (figure 1(e)). T increased almost everywhere except for parts of Northern Australia. Among the 1537 land grids, 87 and 84% exhibit a linear trend that is statistically significant at the 10 and 5% level, respectively. The three T datasets of CRU, GISS and NCDC display very similar warming features in both spatial patterns and

Figure 2. Classification map of (a) 7 and (b) 35 large-scale ecoregions defined based on the climatological EVI values in 2.5° × 2.5° grid boxes over land. Note that among the 1537 land grid boxes between 50°S and 50°N, only those (1338 in total) with annual T_{trend} that is statistically significant ($p < 0.1$) are considered for analysis at the aggregated large-scale ecoregion level (see more detail in the main text).

magnitude (not shown), except for several particular regions in the CRU data (e.g., Amazon and Central Africa) where limited observations were used to interpolate the gridded data (Harris and Jones 2014). Significant warming occurs mostly in arid and semiarid regions such as Northern Africa, Middle East, Northern China, and Western US. EVI (figure 1(d)) and precipitation (figure 1(e)) resemble each other geographically (with a spatial correlation of 0.90; $n = 1338$)—the region with the least amount of precipitation has the least amount of vegetation or vice visa. Overall the warming trend is generally strongest over the driest or least vegetated regions such as the Sahara desert and the Arabian Peninsula.

Figure 2 illustrates the 7 and 35 large-scale ecoregions classified based on the climatology of EVI, representing the range of the least and most ecoregions considered in this study. As expected, most ecoregions are spatially coherent and resemble the geographic distribution of the climatology of precipitation (figure 1(e)). Figure 3 shows regional mean T anomalies from 1979 to 2012 for the three individual T datasets. Four ecoregions were chosen to represent the ones with the least and most amount of vegetation or the driest and wettest climate. In every ecoregion, the three T datasets exhibit similar interannual variability and comparable warming trends that are statistically

significant ($p < 0.001$), with stronger warming rates over drier ecosystems. For example, the warming trend in NCDC is 0.39 ± 0.05 and 0.19 ± 0.03 °C/10 yr for the driest and wettest regions, respectively, in the case of 7 ecoregions. The corresponding values are 0.39 ± 0.06 and 0.21 ± 0.03 °C/10 yr for the 35 ecoregion case. The GISS and CRU data show very similar warming trends as those in NCDC.

Figure 4 shows T_{trend} as a function of $\overline{\text{EVI}}$ in terms of 7 and 35 ecoregions. Evidently, the warming rate depends strongly on ecoregions. T_{trend} increases dramatically with decreasing $\overline{\text{EVI}}$, particularly over very dry areas, indicating the lower the vegetation greenness, the stronger the warming trend. Five different regression lines (exponential, linear, logarithmic, polynomial and power) are fit between T_{trend} and $\overline{\text{EVI}}$ but the negative logarithmic function works best, with $R^2 = 96$ and 89% for the 7 and 35 ecoregions, respectively (figures 4(a) and (b)). Other clarifications of ecoregions (table 1) agree that the negative logarithmic function best describes the $T_{\text{trend}}-\overline{\text{EVI}}$ relationship by ecoregion. Furthermore, the CRU, GISS and NCDC datasets display very similar relationships individually (figures 4(c) and (d)). Note that the R^2 values in CRU are smaller than those in GISS and NCDC because CRU has missing or low-quality data over several data-scarcity regions as mentioned previously.
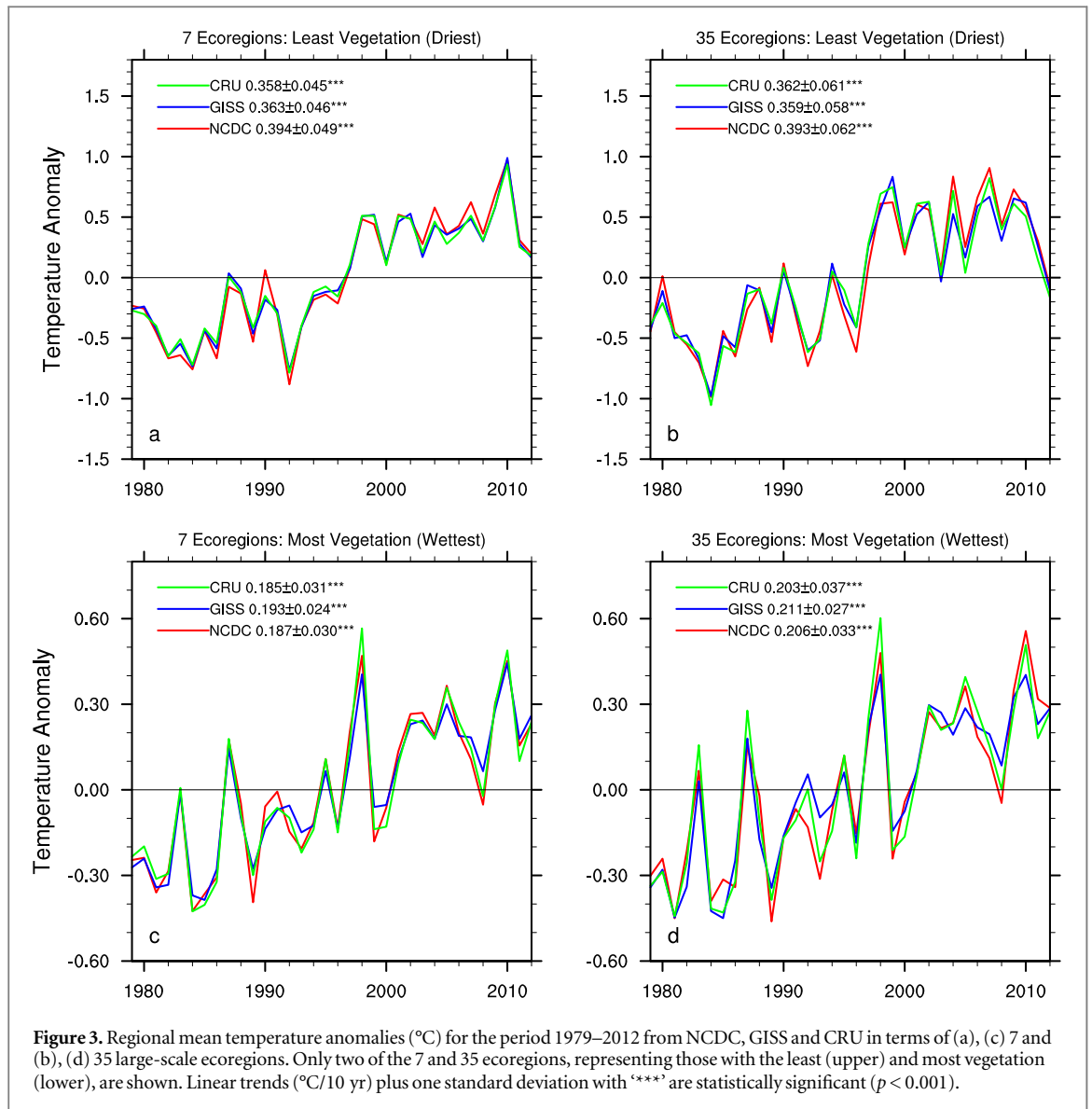
Figure 3. Regional mean temperature anomalies (°C) for the period 1979–2012 from NCDC, GISS and CRU in terms of (a), (c) 7 and (b), (d) 35 large-scale ecoregions. Only two of the 7 and 35 ecoregions, representing those with the least (upper) and most vegetation (lower), are shown. Linear trends (°C/10 yr) plus one standard deviation with '***' are statistically significant ($p < 0.001$).

To examine whether the negative logarithmic $T_{trend}-\overline{EVI}$ relationship varies with observational datasets and depends on how the ecoregions are classified, we perform the same fitting by ecoregion for other ecoregion classifications (table 2) and for each dataset (supplementary table S3). The negative logarithmic fit performs better than the linear fit and this is consistent across all classifications and in all the datasets. The fitted coefficient (A_0) decreases slightly with the increasing number of ecoregions, and so does R^2. When more ecoregions (or $\overline{EVI}$ bins) are considered, R^2 decreases because more small-scale factors affect the spatial variations of T_{trend}. As the estimated trends may be sensitive to start or end points of data record, we also perform the same analyses as done above but consider other study periods (e.g., 1979–2010 and 1981–2012) by changing the start and/or end dates. Again, the negative logarithmic relationship remains robust.

One way to validate the robustness of the above $T_{trend}-\overline{EVI}$ relationship by ecoregion is to simply reconstruct the spatial patterns of T_{trend} from the ecoregion map of EVI clusters (figures 2(a) and (b)) multiplied by the average temperature trend for each of these clusters (figures 4(a) and (b)). If the reconstructed T_{trend} resembles (the first order) the observed trend (figure 1(a)), this supports the idea that the warming rate depends mostly on the ecoregions and the classification of warming rates based on ecoregions is useful. Figure 5 shows the spatial patterns of reconstructed T_{trend}, which exhibit warming patterns similar to the observed at large scales. The strongest warming rates are consistently seen over the driest ecoregions. The spatial correlation at the grid level is 0.55 (between figures 1(a) and 5(a)) and 0.58 (between figures 1(a) and 5(b)), respectively. These correlations are statistically significant at $p < 0.001$ ($n = 1338$).

3.2. Temperature trends in CMIP5 simulations
Figure 1(b) shows the spatial patterns of ALL T_{trend} over land for the period 1979–2012. The warming is
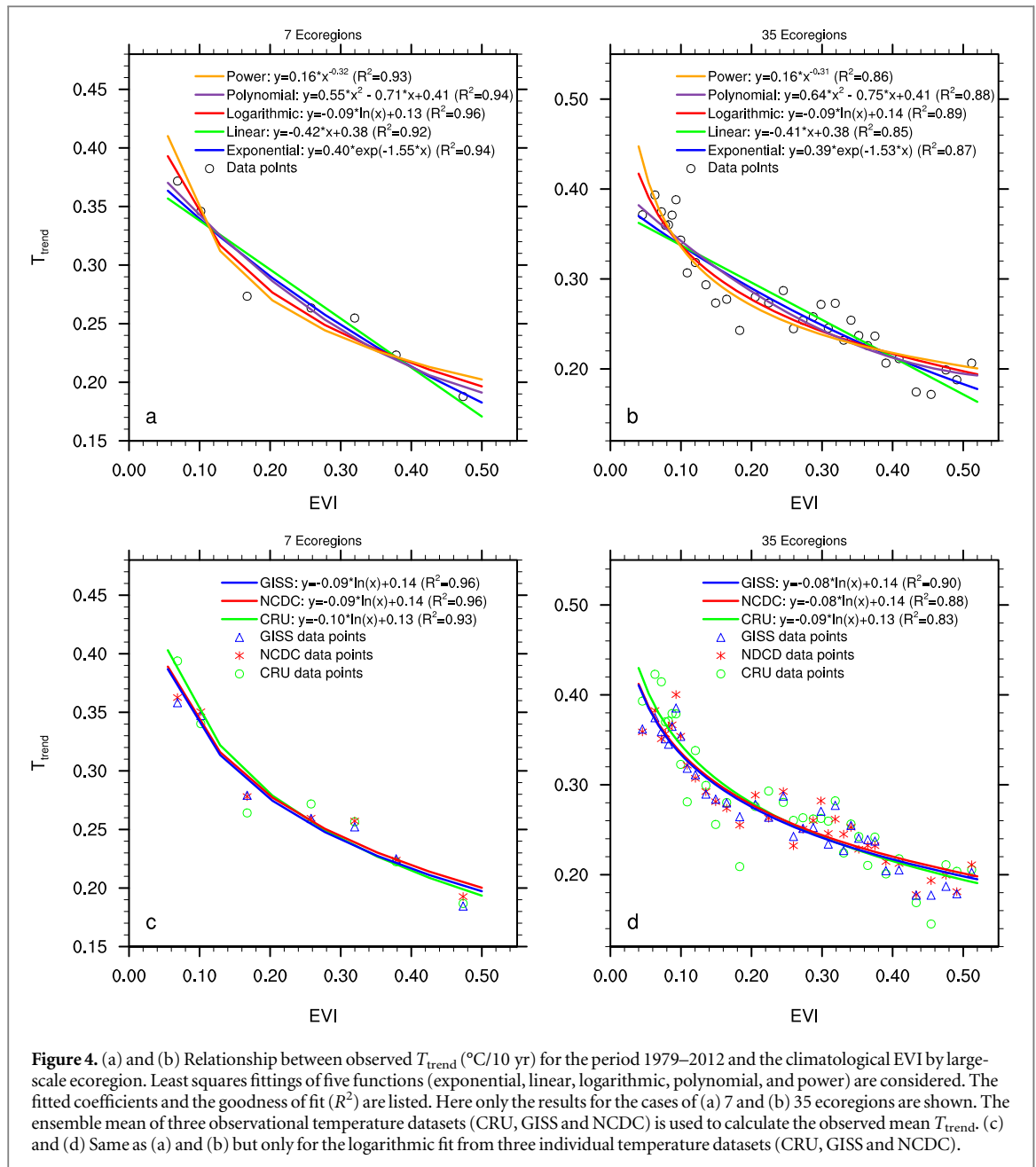
Figure 4. (a) and (b) Relationship between observed T_{trend} (°C/10 yr) for the period 1979–2012 and the climatological EVI by large-scale ecoregion. Least squares fittings of five functions (exponential, linear, logarithmic, polynomial, and power) are considered. The fitted coefficients and the goodness of fit (R^2) are listed. Here only the results for the cases of (a) 7 and (b) 35 ecoregions are shown. The ensemble mean of three observational temperature datasets (CRU, GISS and NCDC) is used to calculate the observed mean T_{trend}. (c) and (d) Same as (a) and (b) but only for the logarithmic fit from three individual temperature datasets (CRU, GISS and NCDC).

Table 1. The goodness of fit (R^2) for different fitting functions between observed T_{trend} (°C/10 yr) and the climatological EVI ($\overline{EVI}$) by large-scale ecoregion.

Ecoregions	Power	Polynomial	Logarithmic	Linear	Exponential
7	0.93	0.94	0.96	0.92	0.95
14	0.90	0.91	0.93	0.88	0.91
21	0.90	0.91	0.93	0.88	0.91
28	0.88	0.89	0.91	0.86	0.89
35	0.86	0.88	0.89	0.85	0.87

The ensemble mean of three observational temperature datasets (CRU, GISS and NCDC) is used to calculate the mean T_{trend}.

ubiquitous and the strongest warming occurs primarily in arid and semi-arid regions such as Northern Africa, Middle East, and Western US. All the land grids (50°S–50°N) exhibit a statistically significant linear trend ($p < 0.05$), which is much higher than the observations. The observed T_{trend}–$\overline{EVI}$ relationship remains true also in ALL (figure 6). The R^2 value for the logarithmic (linear) fit is 99 and 92% (92 and 85%) for the 7 and 35 ecoregions, respectively. Other ecoregion clarifications (table 2) support consistently
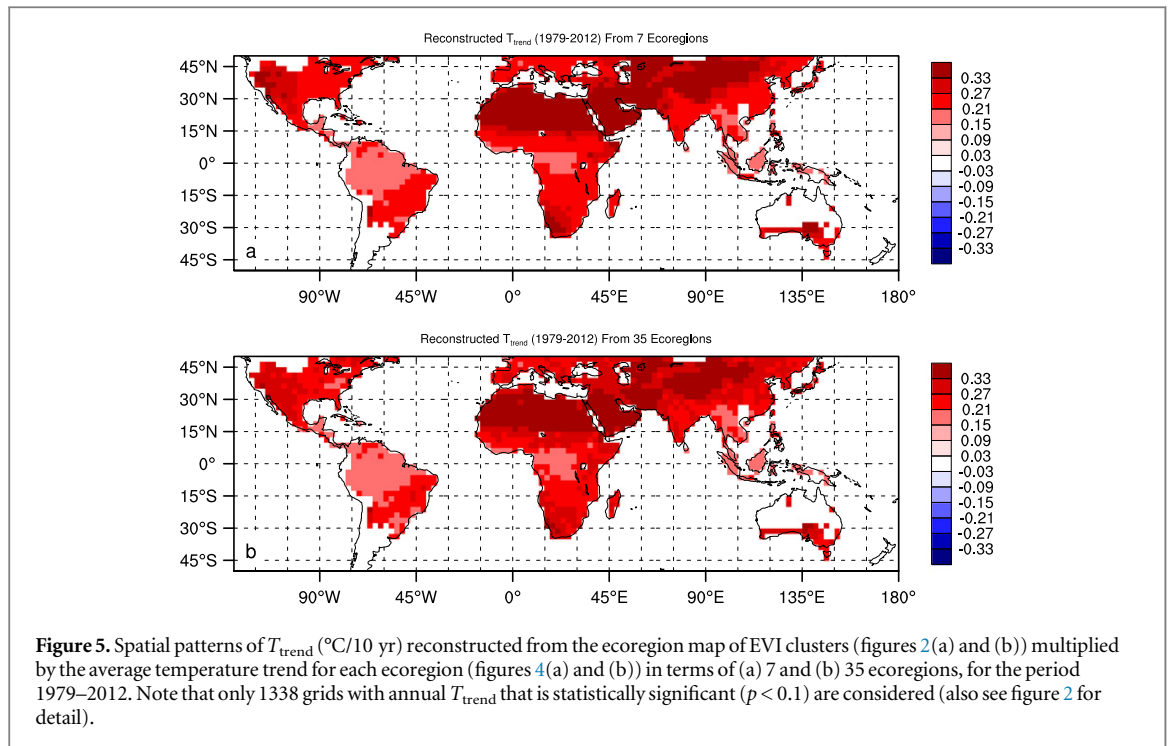
Figure 5. Spatial patterns of T_{trend} (°C/10 yr) reconstructed from the ecoregion map of EVI clusters (figures 2(a) and (b)) multiplied by the average temperature trend for each ecoregion (figures 4(a) and (b)) in terms of (a) 7 and (b) 35 ecoregions, for the period 1979–2012. Note that only 1338 grids with annual T_{trend} that is statistically significant ($p < 0.1$) are considered (also see figure 2 for detail).
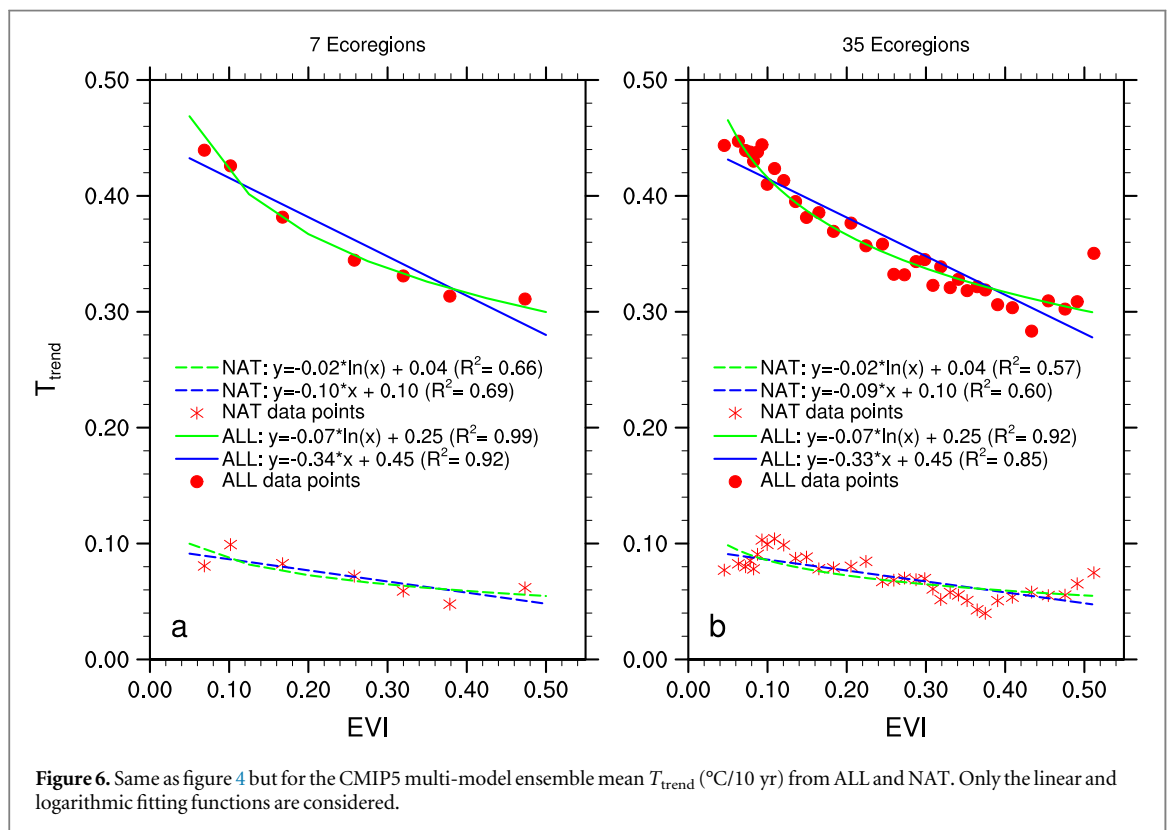

Figure 6. Same as figure 4 but for the CMIP5 multi-model ensemble mean T_{trend} (°C/10 yr) from ALL and NAT. Only the linear and logarithmic fitting functions are considered.

that the negative logarithmic fit better describes the $T_{trend}-\overline{EVI}$ relationship by large-scale ecoregion than the linear fit. Overall ALL largely reproduces the observed warming spatial patterns and the negative logarithmic $T_{trend}-\overline{EVI}$ relationship by ecoregion. At the grid level, the spatial correlation is 0.75 ($n = 1338$) between the observed and ALL T_{trend}, indicating that some regional biases in ALL simulations due to

models' difficulties in simulating T change at small scales.

Figure 1(c) displays the spatial patterns of NAT T_{trend} over land for the period 1979–2005. The warming trend is strongest in several arid and semi-arid zones. For the 1537 land grids (50°S–50°N), only 27 and 13% exhibit a linear trend that is statistically significant at the 10 and 5% level, respectively.

Table 2. The fitted coefficients and goodness of fit (R^2) of the linear and logarithmic fits between $\overline{\text{EVI}}$ and T_{trend} (°C/10 yr) from observations and CMIP5 simulations by large-scale ecoregion.

Ecoregions	$y = A_0 * \overline{\text{EVI}} + C_0$		$y = A_0 * \ln(\overline{\text{EVI}}) + C_0$	
	A_0	R^2	A_0	R^2
	Observed			
7	−0.42	0.92	−0.09	0.96
14	−0.42	0.88	−0.09	0.93
21	−0.42	0.88	−0.09	0.93
28	−0.42	0.86	−0.09	0.91
35	−0.41	0.85	−0.09	0.89
	CMIP5—ALL			
7	−0.34	0.92	−0.07	0.99
14	−0.34	0.89	−0.07	0.96
21	−0.34	0.88	−0.07	0.95
28	−0.33	0.86	−0.07	0.93
35	−0.33	0.85	−0.07	0.92
	CMIP5—NAT			
7	−0.10	0.69	−0.02	0.66
14	−0.09	0.65	−0.02	0.62
21	−0.09	0.63	−0.02	0.60
28	−0.09	0.60	−0.02	0.57
35	−0.09	0.60	−0.02	0.57

The ensemble mean of three observational temperature datasets (CRU, GISS and NCDC) is used to calculate the observed mean T_{trend}.

Figure 7. Histogram of T_{trend} (°C/10 yr) from observations (OBS), ALL and NAT. The ensemble mean of three observational temperature datasets (CRU, GISS and NCDC) is used to calculate the observed mean T_{trend} (OBS-Mean).

The corresponding large-scale $T_{\text{trend}} - \overline{\text{EVI}}$ relationship (figure 6) displays larger warming rates over drier (or lower EVI) ecoregions as shown in ALL, but has a much smaller warming magnitude than ALL. The spatial pattern of T_{trend} (figure 1(c)) and the $T_{\text{trend}} - \overline{\text{EVI}}$ relationships by ecoregion in NAT differ substantially from the observations and ALL (figure 6; table 2), indicating that anthropogenic forcings should play a key role in determining the observed $T_{\text{trend}} - \overline{\text{EVI}}$ relationships.

The histogram of T_{trend} for the CMIP5 ALL and NAT simulations, together with that from the three observational T datasets, is shown in figure 7. In general, ALL T_{trend} is within the observed T_{trend} range but has a narrower distribution skewed to the right (warming) side, indicating higher warming rates and stronger spatial coherence in ALL than observed. This is expected as the multi-model ensemble mean in ALL represents primarily the forced signal (Dai 2013), and ALL slightly overestimates the warming trends for the period 1979–2012 because the simulated T anomalies are higher than observed during the global warming hiatus (IPCC 2013). In contrast, NAT shows small and equal possibilities of cooling and warming trends, which are mostly skewed to the left side (cooling and small warming) and outside the range of ALL simulations and observations, indicating again that the role
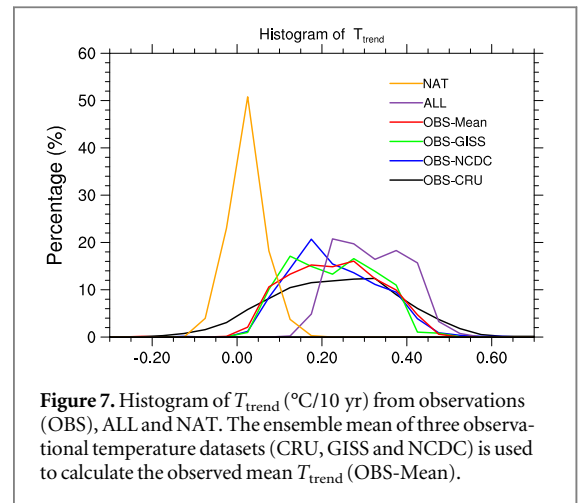
of anthropogenic forcing in reproducing the observed warming patterns.

4. Discussion and conclusions

This paper explores spatial relationships between the observed land surface warming rates and the climatological EVI in terms of large-scale ecoregions for the last three decades. The regional mean temperature trends exhibit significant spatial dependence on the regional mean EVI. In general, the warming rate increases dramatically with decreasing EVI, with the strongest warming rate over the driest ecoregions. When anthropogenic and natural forcings are included, climate models are generally able to reproduce observed major features of the spatial dependence. When only natural forcings are used, none of the observed features are simulated. Furthermore, the temperature changes simulated in NAT are mostly far outside the range of those simulated in ALL and observed. These results indicate stronger warming amplification over drier ecoregions, pointing mainly to human influence.

We focus our analysis mostly on the negative logarithmic $T_{\text{trend}} - \overline{\text{EVI}}$ fit because it generally has the highest R^2 than other fitting functions. However, all fit functions indicate consistently the strongest warming rates over the driest ecosystems for the period 1979–2012. The warming rate of T_{trend} is determined by the magnitude of the surface radiative forcing and any feedbacks involved related to land surface and atmospheric boundary layer processes (Hasselmann 1976, Betts *et al* 1996, Zhou *et al* 2007, 2009, 2010, McNider *et al* 2012, Guo and Dirmeyer 2013, Dirmeyer *et al* 2013, Davy and Esau 2014). Evidently, the finding of the strongest warming in very dry regions needs a new mechanism to explain it. Our further analyses of multiple observational variables, combined with reanalysis data and CMIP5 simulations, could attribute the spatial dependence of warming on ecosystem to much stronger water vapor and ecosystem feedbacks in response to the positive large-scale

GHGs enhanced longwave radiative forcing over drier areas, which will be detailed in future work.

Our results suggest a fundamental pattern of global warming over land that depend on the dryness of ecosystems in mid-and low-latitudes. The ecoregion-dependent warming may reflect primarily the large-scale thermodynamic component of global warming linked to changes in the water and energy cycles over different ecosystems. It is very likely that the reconstructed T_{trend} (figure 5) provides the first order estimate of this pattern and its differences from the observed T_{trend} are related to the dynamical component linked to changes in mean circulation. So this analysis provides a new way to break down the total global warming patterns into the dynamical and thermodynamic components and thus help us to understand whether they reinforce or counteract each other over different ecosystems. For example, the reconstructed T_{trend} from observations (figure 5) resembles the CMIP5 ALL T_{trend} (figure 1(b)) because they share similar large-scale thermodynamic responses and feedbacks to global warming; the stronger warming trend over Central USA and Amazonia in the observations than in the reconstructions have been linked to increases in local drought conditions associated with sea surface temperature patterns (e.g. McCabe *et al* 2004, Harris *et al* 2008), which in turn have been linked to aerosol changes (e.g. Cox *et al* 2008, Booth *et al* 2012). This warming amplification over very dry surfaces might help interpret and attribute global warming and assess climate impacts. The presence of the much stronger warming over arid regions in ALL than in NAT indicates that increasing GHGs may play a crucial role in the enhanced warming in the driest ecosystems. Hence our work points to new potential fingerprints of anthropogenic warming that could be used to further distinguish observed temperature trends from natural variations.

Acknowledgments

References

Adler R F *et al* 2003 The version 2 global precipitation climatology project (GPCP) monthly precipitation analysis (1979-present) *J. Hydrometeor.* **4** 1147–67

Betts A K, Ball J H, Beljaars A C M, Miller M J and Viterbo P A 1996 The land surface–atmosphere interaction: a review based on observational and global modeling perspectives *J. Geophys. Res.* **101** 7209–25

Booth B B B, Dunstone N J, Halloran P R, Andrews T and Bellouin N 2012 Aerosols implicated as a prime driver of twentieth-century North Atlantic climate variability *Nature* **484** 228–32

Cohen J L, Furtado J C, Barlow M, Alexeev V A and Cherry J E 2012 Asymmetric seasonal temperature trends *Geophys. Res. Lett.* **39** L04705

Cox P M, Harris P, Huntingford C, Betts R, Collins M, Jones C, Jupp T, Marengo J and Nobre C A 2008 Increasing risk of Amazon drought due to decreasing aerosol pollution *Nature* **453** 212–5

Dai A 2013 Increasing drought under global warming in observations and models *Nat. Clim. Change* **3** 52–8

Davy R and Esau I 2014 Global climate models' bias in surface temperature trends and variability *Environ. Res. Lett.* **9** 114024

Dirmeyer P A, Jin Y, Singh B and Yan X 2013 Trends in land–atmosphere interactions from CMIP5 simulations *J. Hydrometeorol.* **14** 829–49

Foster G and Rahmstorf S 2011 Global temperature evolution 1979–2010 *Environ. Res. Lett.* **6** 044022

Georgescu M, Lobell D B and Field C B 2011 Direct climate effects of perennial bioenergy crops in the United States *PNAS* **108** 4307–12

Guo Z C and Dirmeyer P A 2013 Interannual variability of land–atmosphere coupling strength *J. Hydrometeor.* **14** 1636–46

Hansen J, Ruedy R, Sato M and Lo K 2010 Global surface temperature change *Rev. Geophys.* **48** RG4004

Harris I, Jones P D, Osborn T J and Lister D H 2014 Updated high-resolution grids of monthly climatic observations—the CRU TS 3.1 data set *Int. J. Climatol.* **34** 623–42

Harris P P, Huntingford C and Cox P M 2008 Amazon basin climate under global warming: the role of the sea-surface temperature *Phil. Trans. R. Soc.* B **363** 1753–9

Hasselmann K 1976 Stochastic climate models : 1. Theory *Tellus* **28** 473–85

Huete A, Didan K, Miura T, Rodriguez E P, Gao X and Ferreira L G 2002 Overview of the radiometric and biophysical performance of the MODIS vegetation indices *Remote Sens. Environ.* **83** 195–213

IPCC 2013 *Climate Change 2013 : The Physical Science Basis the contribution of Working Group I to the Fifth Assessment Report of the Intergovernmental Panel on Climate Change* (Cambridge: Cambridge University Press)

Jeong S J, Ho C H and Jeong J H 2009 Increase in vegetation greenness and decrease in springtime warming over East Asia *Geophy. Res. Lett.* **36** L02710

Koster R D *et al* 2004 Regions of strong coupling between soil moisture and precipitation *Science* **305** 1138–40

Koster R D, Schubert S D and Suarez M J 2009 Analyzing the concurrence of meteorological droughts and warm periods, with implications for the determination of the evaporative regime *J. Climate* **22** 3331–3141

Lim Y-K, Cai M, Kalnay E and Zhou L 2005 Observational evidence of sensitivity of surface climate changes to land types and urbanization *Geophy. Res. Lett.* **32** L22712

Lu J and Cai M 2010 Quantifying contributions to polar warming amplification in an idealized coupled general circulation model *Clim. Dyn.* **34** 669–87

McCabe G J, Palecki M A and Betancourt J L 2004 Pacific and Atlantic Ocean influences on multidecadal drought frequency in the United States *Proc. Natl Acad. Sci. USA* **101** 4136–41

McNider R T, Steeneveld G J, Holtslag A A M, Pielke R A Sr, Mackaro S, Pour-Biazar A, Walters J, Nair U and Christy J 2012 Response and sensitivity of the nocturnal boundary layer over land to added longwave radiative forcing *J. Geophys. Res.* **117** D14106

Naud C M, Chen Y-H, Rangwala I and Miller J R 2013 Sensitivity of downward longwave surface radiation to moisture and cloud changes in a high elevation region *J. Geophys. Res.* **118** 072–10

Nagler P L, Scott R L, Westenburg C, Cleverly J R, Glenn E P and Huete A R 2005 Evapotranspiration on western US rivers estimated using the enhanced vegetation indices from MODIS and data from eddy covariance and Bowen ratio flux towers *Remote Sens. Environ.* **97** 337–51

Rangwala I, Sinsky E and Miller R J 2013 Amplified warming projections for high altitude regions of the Northern hemisphere mid-latitudes from CMIP5 models *Environ. Res. Lett.* **8** 024040

Simmons A J, Willett K M, Jones P D, Thorne P W and Dee D P 2010 Low-frequency variations in surface atmospheric humidity, temperature, and precipitation: inferences from reanalyses and monthly gridded observational data sets *J. Geophys. Res.* **115** D01110

Suzuki R and Masuda K 2004 Interannual co-variability found in evapotranspiration and satellite-derived vegetation indices over Northern Asia *J. Meteorol. Soc. Japan.* **82** 1233–41

Tang Q H and Leng G Y 2013 Changes in cloud cover, precipitation and summer temperature in North America from 1982–2009 *J. Climate* **26** 1733–44

Taylor K E, Stouffer R J and Meehl G A 2012 An overview of CMIP5 and the experiment design *Bull. Am. Meteorol. Soc.* **93** 485–98

Thorne P W, Lanzante J R, Peterson T C, Seidel D J and Shine K P 2011 Tropospheric temperature trends: history of an ongoing controversy *WIREs Clim. Change* **2** 66–88

Vose R S *et al* 2012 NOAA's merged land–ocean surface temperature analysis *Bull. Amer. Meteor. Soc.* **93** 1677–85

Wang K C and Dickinson R E 2012 A review of global terrestrial evapotranspiration: observation, modeling, climatology, and climatic variability *Rev. Geophys.* **50** RG2005

Zhou L, Dai A, Dai Y, Vose R S, Zou C-Z, Tian Y and Chen H 2009 Spatial dependence of diurnal temperature range trends on precipitation from 1950 to 2004 *Clim. Dyn.* **32** 429–40

Zhou L, Dickinson R E, Tian Y and Vose R S 2007 Impact of vegetation removal and soil aridation on diurnal temperature range in a semiarid region—application to the Sahel *Proc. Natl. Acad. Sci. USA* **104** 17937–42

Zhou L, Dickinson R E, Dai A and Dirmeyer P 2010 Detection and attribution of anthropogenic forcing to diurnal temperature range changes from 1950 to 1999: comparing multi-model simulations with observations *Clim. Dyn.* **35** 1289–307